CHALMERS
UNIVERSITY OF TECHNOLOGY

Development of powder bed fusion–laser beam process for AISI 4140, 4340 and 8620 low-alloy steel

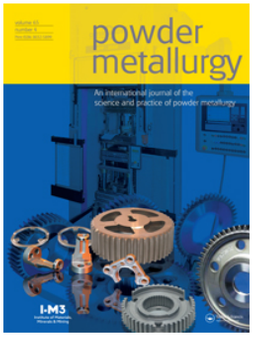

Powder Metallurgy

ISSN: (Print) (Online) Journal homepage: https://www.tandfonline.com/loi/ypom20

Development of powder bed fusion – laser beam process for AISI 4140, 4340 and 8620 low-alloy steel

William Hearn, Peter Harlin & Eduard Hryha

To cite this article: William Hearn, Peter Harlin & Eduard Hryha (2022): Development of powder bed fusion – laser beam process for AISI 4140, 4340 and 8620 low-alloy steel, Powder Metallurgy, DOI: 10.1080/00325899.2022.2134083

To link to this article: https://doi.org/10.1080/00325899.2022.2134083

Published online: 17 Oct 2022.

POWDER METALLURGY
https://doi.org/10.1080/00325899.2022.2134083

I·M3 Institute of Materials, Minerals & Mining
Taylor & Francis Taylor & Francis Group

Development of powder bed fusion – laser beam process for AISI 4140, 4340 and 8620 low-alloy steel

William Hearn [a], Peter Harlin[b] and Eduard Hryha[a]

[a]Department of Industrial and Materials Science, Chalmers University of Technology, Gothenburg, Sweden; [b]Sandvik Additive Manufacturing, Sandviken, Sweden

ABSTRACT

This study focuses on process development and mechanical property evaluation of AISI 4140, 4340 and 8620 low-alloy steel produced by powder bed fusion – laser beam (PBF-LB). Process development found that increasing the build plate preheating temperature to 180°C improved processability, as it mitigated lack of fusion and cold cracking defects. Subsequent mechanical testing found that the low-alloy steels achieved a high ultimate tensile strength (4140:~1400 MPa, 4340:~1500 MPa, 8620:~1100 MPa), impact toughness (4140:~90–100 J, 4340:~60–70 J, 8620:~150–175 J) and elongation (4140:~14%, 4340:~14%, 8620:~14–15%) that met or exceeded the ASTM standards. Mechanical testing also revealed limited directional anisotropy that was attributed to low levels of internal defects (< 0.1%), small grains with weak crystallographic texture and improved tempering due to build plate preheating and post PBF-LB stress relief. This indicates that with adequate process development, low-alloy steels produced by PBF-LB can meet or exceed the performance of conventionally produced alloys.

ARTICLE HISTORY
Received 11 July 2022
Accepted 1 October 2022

KEYWORDS
Additive manufacturing; powder bed fusion; low-alloy steel; processing; build plate preheating; microstructure; properties

Introduction

Powder bed fusion – laser beam (PBF-LB) is an additive manufacturing technique that involves selective fusion of a powder-bed using a high-powered laser source. The precision of the process, along with its ability to directly print CAD designs, has made it a suitable method to produce near-net shape metallic components [1]. Additionally, it offers a more sustainable processing route when compared to conventional manufacturing techniques [2]. Despite this, PBF-LB still lacks wide-spread adoption as a manufacturing technique, which can be partially attributed to the scarcity of approved alloys for the process.

Martensitic low-alloy steels are alloys of growing interest for PBF-LB as they provide high strength, wear resistance, toughness and hardness while maintaining a relatively low materials cost [3,4]. Additionally, the adoption of these alloys would expand the use of PBF-LB to the automotive, railway and pipe-line industries [4]. Still, to the authors knowledge these alloys have yet to become commercially available for the process.

The lack of martensitic low-alloy steel in PBF-LB stems from the difficulty of processing these alloys defect-free and high-density. One of the major issues is related to their high carbon content (0.3–0.5 wt.% C), which induces cracking within the material due to the formation of brittle martensite along with the presence of large residual stresses. Additionally, there are generic issues during PBF-LB (e.g. keyholes pores and lack of fusion defects) that can lead to a reduction in performance when compared to conventionally produced material and induce anisotropic behaviour [5–7]. Overall, these issues have put into question the viability of martensitic low-alloy steel when using PBF-LB.

In order to adopt these alloys for PBF-LB, detailed process development is required in combination with mechanical property testing. To date, limited data on this subject is available in the literature, with process development of martensitic low-alloy steel primarily involving single-track experiments [8–10] and the production of specimens at specific sets of processing parameters [6,7,11,12]. An important parameter that has yet to be examined in adequate detail is the build plate preheating temperature (BPT), which has improved the processing of carbon-containing tool steels during PBF-LB [13–15].

To fill this knowledge gap, the current study used a combined approach of process development and mechanical property testing to assess the performance of AISI 4140, 4340 and 8620 low-alloy steel

CONTACT William Hearn hearn@chalmers.se Department of Industrial and Materials Science, Chalmers University of Technology, SE-41296 Gothenburg, Sweden

when using PBF-LB. Initial process development involved the printing of specimens at BPTs of 25°C, 100°C and 180°C, across volumetric energy densities of 60–200 J/mm^3. This range of parameters was evaluated to not only determine the conditions that achieved defect-free and high-density specimens (> 99.8%) but also to determine the largest processing window to help ensure process robustness. Using the best parameters, tensile and Charpy impact toughness specimens were produced and tested in orientations horizontal and vertical to the build plate. From these analyses, it was possible to measure a material response for each of the alloys, that made it possible to evaluate the feasibility and performance of martensitic low-alloy steel when using PBF-LB.

Materials and methods

Materials & processing

Pre-alloyed, inert gas atomised powder supplied by Sandvik Osprey™ was used as the feedstock material in this study. The chemical composition of each powder grade is listed in Table 1, while the powder particle size distribution is listed in Table 2. Examination of the powder particles revealed a circular morphology for each alloy, see Figure 1.

Powder bed fusion – laser beam (PBF-LB) was carried out using an EOS M290 machine (EOS GmbH, Germany). This machine is equipped with an Yb-fibre laser that has a maximum power of 400 W and a beam diameter of ~100 µm. During laser exposure a 5 mm stripe scan pattern and a 67° scan rotation angle was employed, along with no outer-skin or top-skin parameters. During processing an oxygen level of ~0.1% was maintained within the building chamber using Ar gas.

To vary the processing conditions during PBF-LB the volumetric energy density (VED) was utilised. This combined processing parameter provides an estimation of the energy input and is a function of the scan speed (v), hatch spacing (h), layer thickness (t) and laser power (P):

Production of the $10 \times 10 \times 10$ mm^3 cube specimens was done at build plate preheating temperatures (BPT) of 25°C, 100°C and 180°C across VEDs of 60–200 J/mm^3. To vary the VED the scan speed was changed while maintaining a constant laser power (170 W), hatch spacing (70 µm) and layer thickness (20 µm). Production of the tensile and Charpy specimens was carried out using a BPT of 180°C and a VED of 120 J/mm^3 following the results from process development.

Metallography

Cube and select mechanical property specimens were sectioned along the XZ direction, where the Z-direction related to the building direction, while the X-direction related to the direction of gas flow. Afterwards, these specimens were mounted and polished using a Struers TegraPol machine (Struers, Denmark). After polishing selected specimens were further etched with Nital (3%).

Light optical microscopy (OM) was conducted using a Zeiss Axiovision 7 Light Optical Microscope (Carl Zeiss AG, Germany). To measure the specimen density, OM images of unetched specimen cross-sections were analysed using ImageJ software [16]. This first involved cropping and converting the images to a binary format to distinguish the defects from the specimen bulk. After this was completed, ImageJ could measure the area percentage of defects and determine the specimen density. OM imaging was also used to estimate the melt pool depth, which was done by measuring the depth of the top layer in etched specimen cross-sections. These measurements are described in more detail during previous work by the authors [17].

Scanning electron microscopy was carried out using a Leo Gemini 1550 high-resolution SEM (Carl Zeiss AG, Germany). The mentioned SEM was also equipped with an Oxford Instruments Nordyls II electron backscatter diffraction (EBSD) detector that was operated at an accelerating voltage of 20 kV, a magnification of 1 kx and a step size of 0.1 µm. Prior to EBSD, specimens were further polished using OPU suspension. From the collected EBSD data, reconstruction of the parent austenite grains was carried out using MTEX software that utilised the ORTools function library [18].

Mechanical testing

Specimens for tensile testing were initially produced as 57 mm×8 mm diameter rods, in orientations horizontal and vertical to the build plate. Prior to removal from the build plate, these specimens underwent stress relief at 200°C for 1 h. After removal, they were

Table 1. Composition of the AISI 4140, 4340 and 8620 low-alloy steel powders.

	C	Ni	Cr	Mo	Mn	Si
AISI 4140	0.38	–	1.10	0.23	0.77	0.22
AISI 4340	0.43	1.90	0.90	0.30	0.60	0.17
AISI 8620	0.22	0.60	0.50	0.22	0.70	0.32

Table 2. Particle size distribution of the AISI 4140, 4340 and 8620 low-alloy steel powders.

	D_{10} (µm)	D_{50} (µm)	D_{90} (µm)
AISI 4140	18.6	31.1	52.2
AISI 4340	18.0	31.9	55.6
AISI 8620	24.9	44.6	71.1

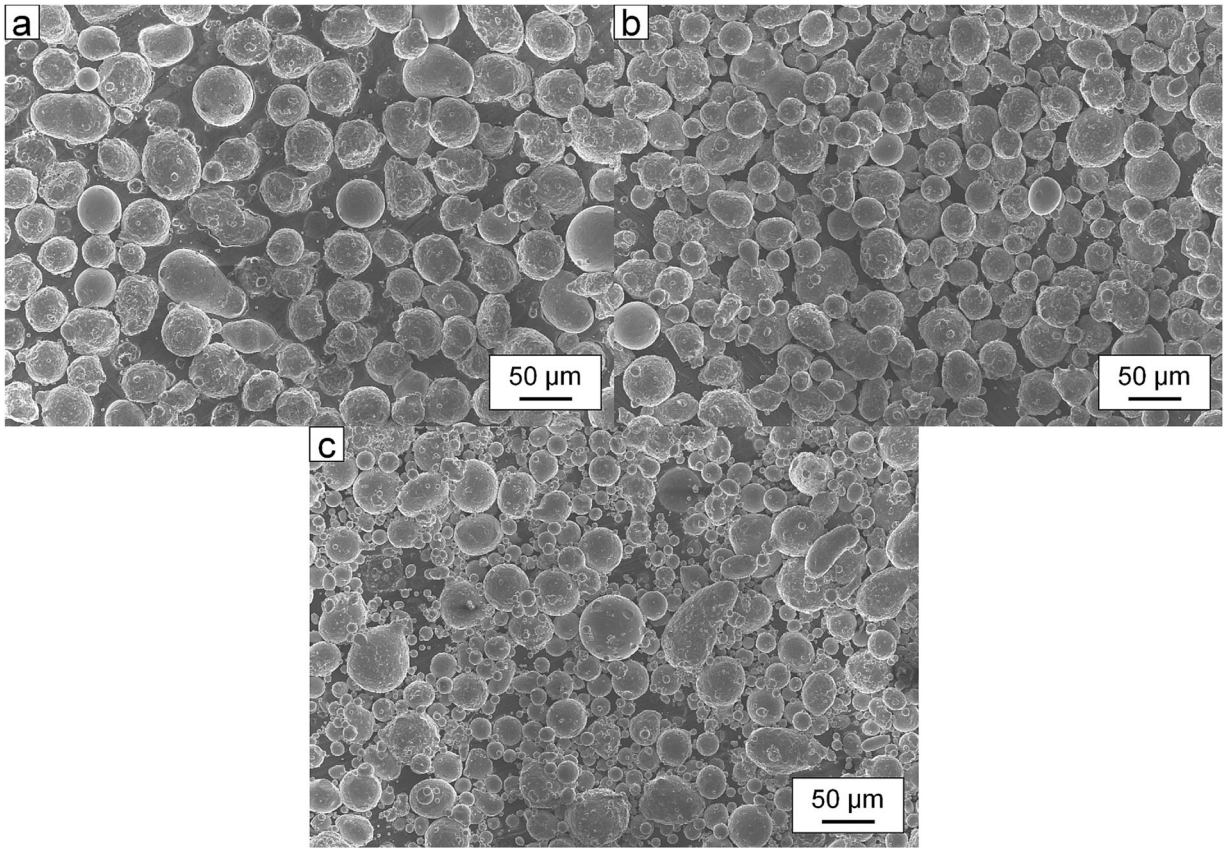

Figure 1. SEM images of the inert gas atomised powders from the: (a) AISI 4140 alloy, (b) AISI 4340 alloy, (c) AISI 8620 alloy.

machined to tensile specimens with a gauge diameter of 4 mm and a gauge length of 20 mm following the ASTM E8M standard [19]. During tensile testing a strain rate of 2.5×10^{-4} s^{-1} was maintained until 1.7% elongation to determine the Rp0.2. After this elongation was achieved, the strain rate was increased to 0.005 per second until fracture. This was done to reduce testing time and was in accordance with the ASTM E8M standard [19]. Tensile testing was carried out at room temperature using an Instron 4505 machine (Instron, USA). For each low-alloy steel and each orientation 3 specimens were tested.

Charpy v-notch impact toughness specimens were initially produced as 12.5 mm × 15.5 mm × 59.5 mm blocks, in orientations horizontal and vertical to the build plate. Prior to removal from the build plate, these specimens underwent stress relief at 200°C for 1 h. After removal, they were machined to 10 mm × 10 mm × 55 mm with the v-notch following the ASTM 2298 standard [20]. Testing of these specimens was conducted at room temperature using a Zwick PSW 750 machine (Zwick Roell Group, USA). For each low-alloy steel and each orientation 3 specimens were tested.

Vickers hardness indentations were performed using a DuraScan 70-G5 machine (EMCO-TEST GmbH, Austria) on cuboid and Charpy specimens. Measurements on cube specimens involved sixteen HV10 indentations, oriented in a 4 × 4 pattern, with each indentation being spaced 2 mm apart. Hardness measurements on the horizontal Charpy specimens involved 182 HV10 indentations, oriented in a 7 × 26 pattern, with each indentation being spaced 2 mm apart. While hardness measurements on the vertical Charpy specimens involved 49 HV10 indentations, oriented in a 7 × 7 pattern, with each indentation being spaced 2 mm apart.

Results

Process development

Effect of VED & BPT on porosity

The specimen density of the low-alloy steels was connected to the VED, see Figure 2. At low VED (Region I), cross-sections revealed numerous lack of fusion pores, see Figure 3(a,b), that contributed to low densities (< 99.5%). These defects formed as the energy input was insufficient to achieve proper bonding between layers and melt tracks. As the VED increased, lack of fusion porosity steadily decreased, see Figure 4. This was due to an increased size of the melt pool, see Figure 5, which helped to improve material bonding. Once higher VEDs were applied minimal porosity was observed within the specimens (Region II), leading to high densities (> 99.8%), see Figure 3(c,d).

The BPT also influenced specimen density, see Figure 2, as increasing this temperature limited lack

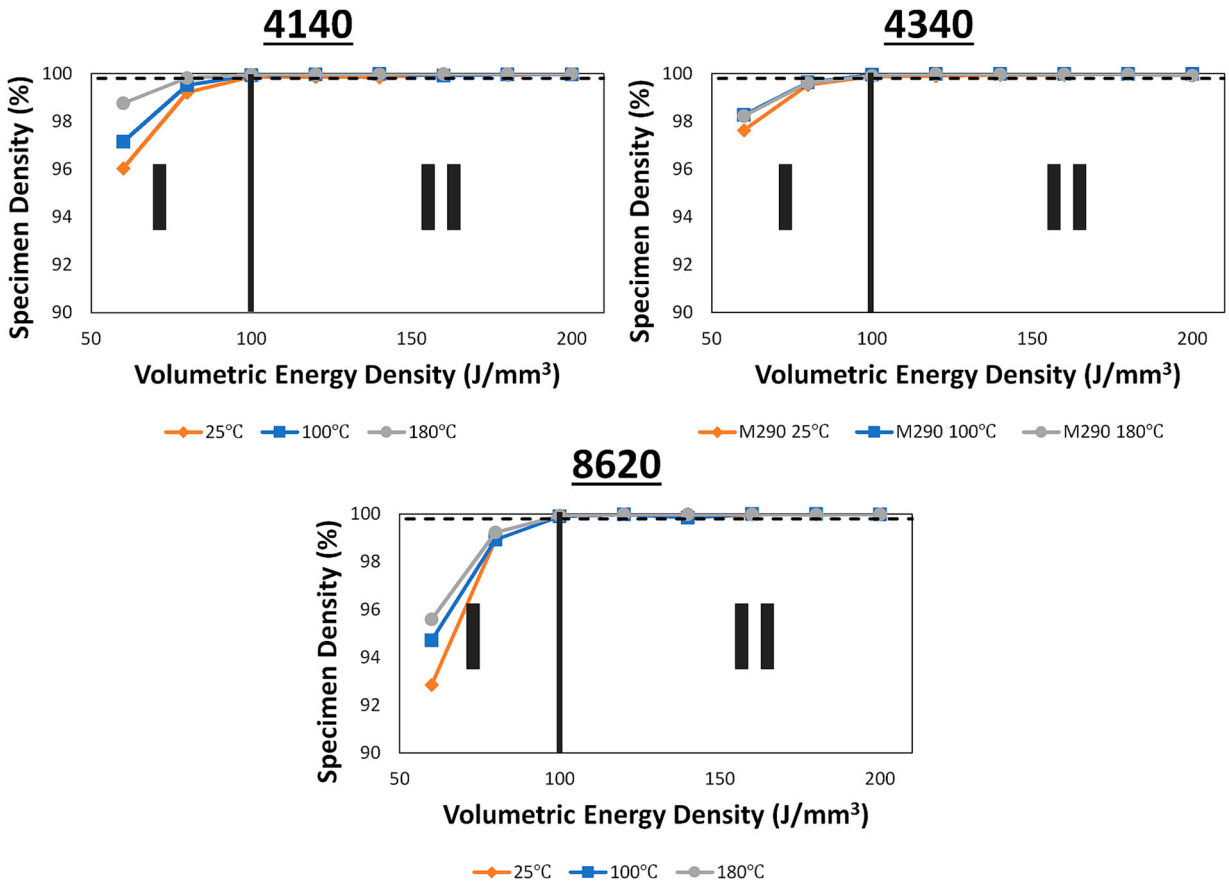

Figure 2. Specimen density as a function of the VED for the AISI 4140, 4340 and 8620 alloys. Marked areas (I and II) represent different processing regions, where specimens within Region II achieved densities > 99.8%. A density of 99.8% is indicated in each of the graphs using a dashed line.

of fusion porosity within the specimens, see Figure 4. This change was due to a higher ambient temperature during processing, which improved material bonding. Additionally, there was an increase in the melt pool depth, see Figure 5, which also enhanced material bonding. Despite these improvements, an increase in the BPT did not noticeably alter the processing range of high-density specimens (> 99.8%), as Region II for the AISI 4340 and 8620 alloys remained unchanged as the temperature increased. While increasing the BPT to 180°C reduced the lower limit of Region II from 100 to 80 J/mm^3 for the AISI 4140 alloy.

Effect of VED & BPT on cold cracking

Within some of the higher carbon low-alloy steels (AISI 4140 and 4340) cracking defects were observed, see Figure 4. These cracks primarily formed at the side surface and grew inwards perpendicular to the building direction. This type of defect is related to a cold cracking phenomenon that has been described previously in works by Hearn et al [17,21]. The mentioned cracking was not observed for the AISI 8620 alloy as this alloy had a much lower carbon content (0.22 wt.%), making it more ductile and thus less susceptible to form these defects.

Cold cracking within the AISI 4140 and 4340 alloys could be mitigated by adjusting the VED or the BPT as this defect was not observed in specimens produced at high VED or at high BPT, see Table 3. This is in part due to the reduction in hardness as both parameters increased, see Figure 5. The reduction in hardness with increasing BPT is connected to a higher ambient temperature during processing which improves martensite tempering. As for the reduction in cracking with increasing VED, this is connected to the larger size of the melt pool, see Figure 5, which reduces the rate of heat dissipation from the solidifying material [22], lowering the speed of heat extraction and increasing the level of martensite tempering. Out of these parameters a BPT of 180°C had the most prominent effect, as under these conditions no cracks were observed in any of the produced specimens.

Processing windows for high-Density, defect-free specimens

From these results, processing windows were established for each low-alloy steel that produced defect-free and high density (> 99.8%) specimens, see Figure 6. For the AISI 8620 alloy, the size of the processing window remained unchanged as the BPT increased as this alloy did not suffer from cold cracking defects. As for the AISI 4140 and 4340 alloys, the size of the processing window increased with increasing BPT due to the reduction in cold cracking. From these findings,

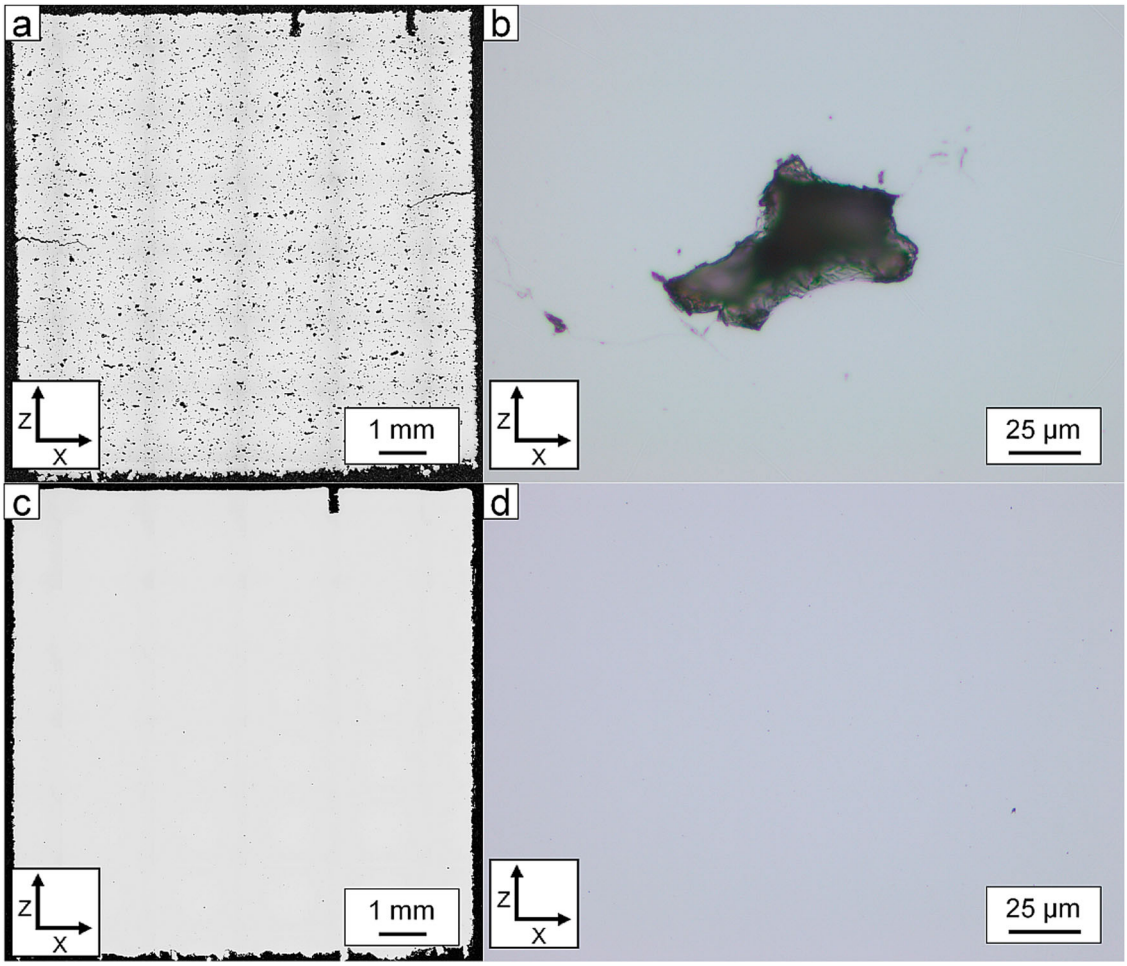

Figure 3. (a) Noticeable lack of fusion porosity in an AISI 4140 alloy specimen produced at 60 J/mm^3 using a BPT of 25°C. (b) Higher magnification of (a) revealed the irregular shape characteristic of these lack of fusion pores. (c) Example of a high-density (> 99.8%) AISI 4340 alloy specimen produced at 140 J/mm^3 using a BPT of 100°C. (d) Higher magnification of (c) revealed minimal porosity within said specimen.

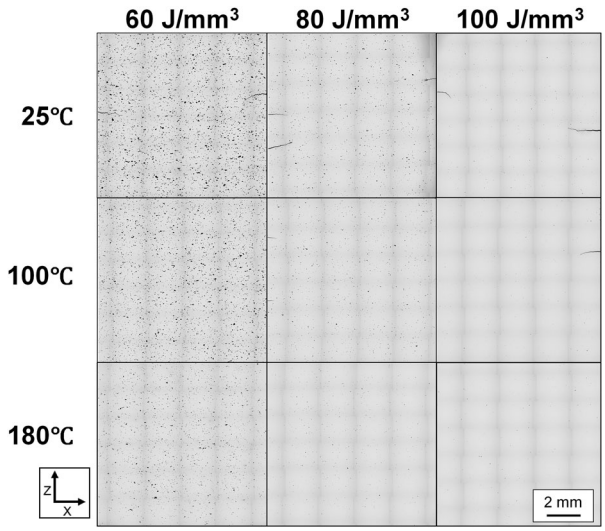

Figure 4. Cross-sections of AISI 4140 alloy specimens produced at VEDs of 60, 80, 100 J/mm^3 and BPTs of 25°C, 100°C, 180°C. At 60 J/mm^3 noticeable lack of fusion porosity was observed in all specimens regardless of the BPT. Additionally, in specimens produced at 25°C and 100°C cracking defects were observed.

the most robust processing window was found at a BPT of 180°C as this temperature provided the largest range of VEDs that achieved high-density and defect-free specimens. Consequently, the mentioned BPT, along with a VED of 120 J/mm^3 was chosen to produce the mechanical property specimens.

Mechanical properties

Tensile and Charpy impact toughness specimens were tested in orientations vertical and horizontal to the build plate. The results of this testing have been summarised in Table 4. Generally, the horizontal specimens performed slightly better than the vertical specimens. However, the level of anisotropy between the two orientations was limited as the difference in yield strength, ultimate tensile strength, elongation, area reduction, young's modulus and hardness, was below 10%. The largest difference between the orientations was observed from impact toughness testing, where the horizontal specimens outperformed the vertical specimens by approximately 8–17%.

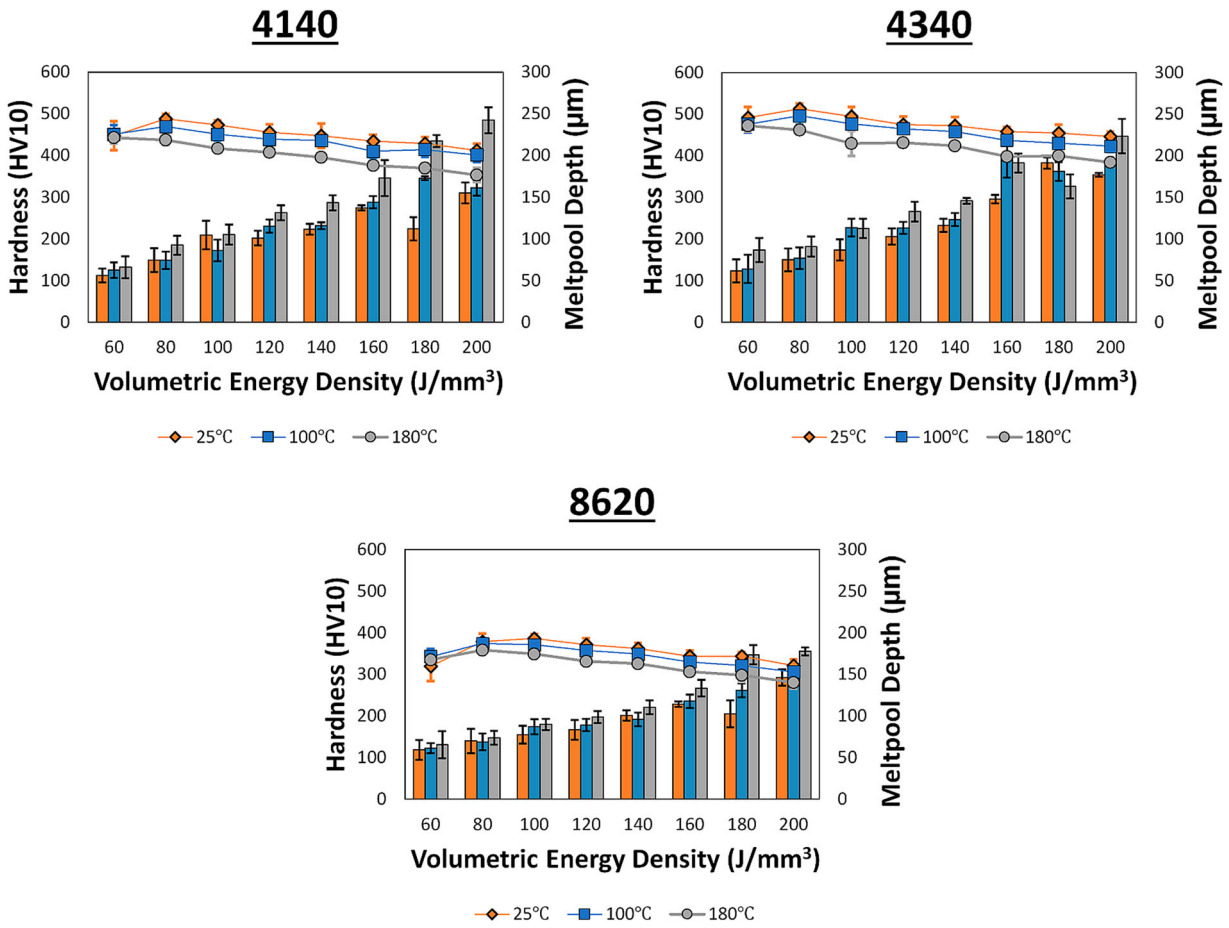

Figure 5. Change in specimen hardness and melt pool depth as a function of the VED and BPT for the AISI 4140, 4340 and 8620 alloys. Hardness is indicated as a scatter plot while the melt pool depth is indicated as a bar chart.

Additional analysis of the stress–strain curves in Figure 7 indicated ductile behaviour for each low-alloy steel. This was corroborated by observations of the tensile fracture surfaces, as macro-observations revealed a cup and cone fracture mode, while micro-observations revealed the fine dispersion of dimples, see Figure 8. Similar ductile features were observed on the fracture surfaces of the Charpy specimens, as macro-observations revealed the presence of shear lips, while micro-observations revealed the presence of fine dimples, see Figure 9. On the tensile and Charpy fracture surfaces only a few scattered pores were observed. Additionally, some secondary cracks were observed in the AISI 4140 and 4340 alloys.

Microstructure

Optical microscopy (OM) revealed a martensitic microstructure within the specimens, see Figure 10. Further hardness measurements found that this martensite was noticeably tempered, see Table 4, as the hardness was similar to conventionally quenched and tempered low-alloy steel [17]. SEM revealed a collection of fine martensite laths, that became more prominent as the carbon content of the alloys increased, see Figure 10. In between these martensite laths, numerous fine precipitates were observed that were less than 100 nm in size.

Results from EBSD are presented in Figure 11. Examination of the band contrast found that the boundaries of the deposited melt tracks had the lowest indexing, as these regions contained many fine grains as well as grain boundaries. Reconstruction of the parent austenite grains found that they were predominantly composed of small columnar grains, along with a few equiaxed grains. In terms of their orientation, they were somewhat aligned with the building direction, however a distinct crystallographic texture was not observed. Inverse pole figure mapping of martensite also revealed a lack of crystallographic texture. This was reinforced from the pole figure mapping, see Figure 12, where a relatively random orientation was observed for each low-alloy steel.

Table 3. VED required to avoid cold cracking in AISI 4140, 4340 and 8620 alloys at each BPT.

	AISI 4140	AISI 4340	AISI 8620
25°C	200 J/mm^3	180 J/mm^3	N/A
100°C	140 J/mm^3	140 J/mm^3	N/A
180°C	N/A	N/A	N/A

Discussion

In this study, process development of defect-free and high-density AISI 4140, 4340 and 8620 steel was

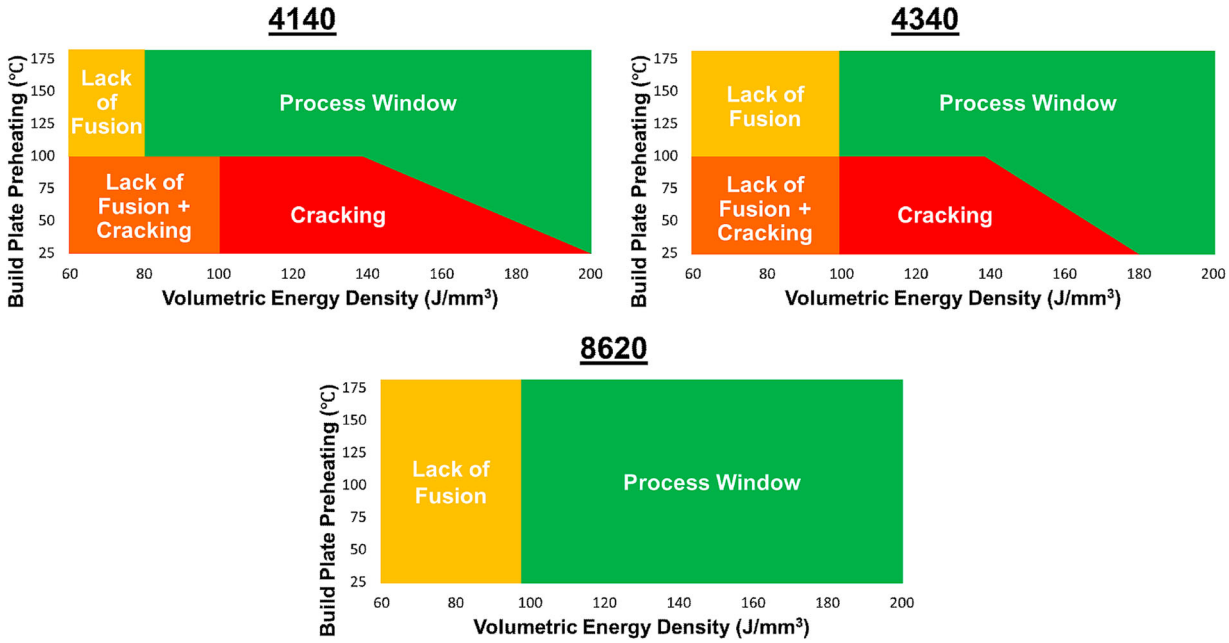

Figure 6. Processing window for the AISI 4140, 4340 and 8620 alloys as a function of the BPT and VED. Samples produced within the process window (green region) were crack-free and high-density (> 99.8%).

Table 4. Results from mechanical property testing of each low-alloy steel.

	YS (MPa)	UTS (MPa)	Elongation (%)	RA (%)	YM (GPa)	Impact (J)	HV 10
4140V	1240 ± 11	1400 ± 9	14.2 ± 0.2	60 ± 1	218 ± 3	92 ± 7	450 ± 10
4140H	1300 ± 19	1420 ± 26	13.9 ± 0.1	63 ± 1	225 ± 3	100 ± 3	432 ± 9
4340V	1230 ± 11	1510 ± 23	14.1 ± 1.0	50 ± 5	209 ± 14	61 ± 3	448 ± 7
4340H	1330 ± 9	1510 ± 23	14.3 ± 0.4	58 ± 2	218 ± 4	71 ± 3	445 ± 7
8620V	1040 ± 7	1090 ± 10	13.8 ± 0.8	65 ± 2	228 ± 2	148 ± 16	343 ± 7
8620H	1070 ± 10	1120 ± 12	15.2 ± 0.8	69 ± 1	228 ± 5	174 ± 12	345 ± 6

Note: Specimens produced in orientations vertical and horizontal to the build plate have been denoted as V and H respectively.

carried out at BPTs of 25°C, 100°C and 180°C. Analysis indicated that increasing the BPT could mitigate the formation of two common defects. The first were lack of fusion pores, which were less likely to form at higher BPT due to improvements in the heat input and melt pool depth. This corresponds to previous findings by Mertens et al. with H13 tool steel [14], who showed that increasing the BPT could improve material densification during PBF-LB. Increasing the BPT also mitigated the formation of cold cracking in alloys with higher carbon content (e.g. AISI 4140 and 4340) as it enhanced martensite tempering during PBF-LB. Increasing the BPT is also likely to reduce residual stress within the material, further reducing the crack susceptibility. Reported studies on carbon-containing tool steel found that increasing the preheating temperature to 200°C would lower the level of residual stress [23,24] and the maximum part deflection [24], supporting this hypothesis. These results indicate that preheating of the build plate is an important processing parameter during PBF-LB that helps produce defect-free and high-density low-alloy steel specimens.

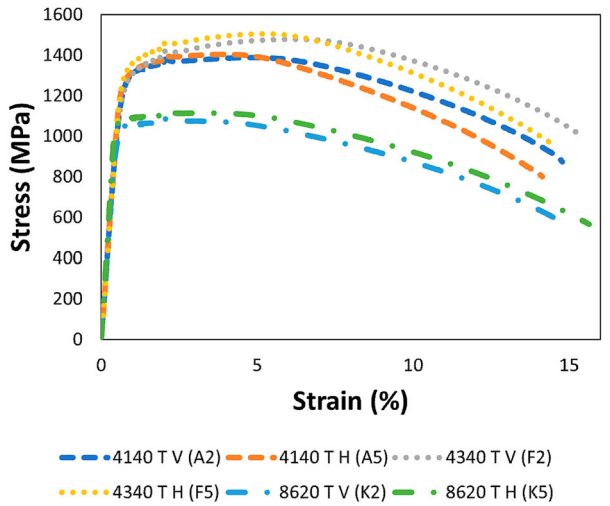

Figure 7. Characteristic engineering stress vs. strain curves for the AISI 4140, 4340 and 8620 alloys produced in orientations vertical and horizontal to the build plate.

After process development, mechanical testing of defect-free and high-density specimens was carried out for each low-alloy steel. Said testing found that the specimens achieved high strength, area reduction and impact toughness that exceeded the ASTM standards, along with solid levels of elongation that fell within the ASTM standards, see Figure 13. The high

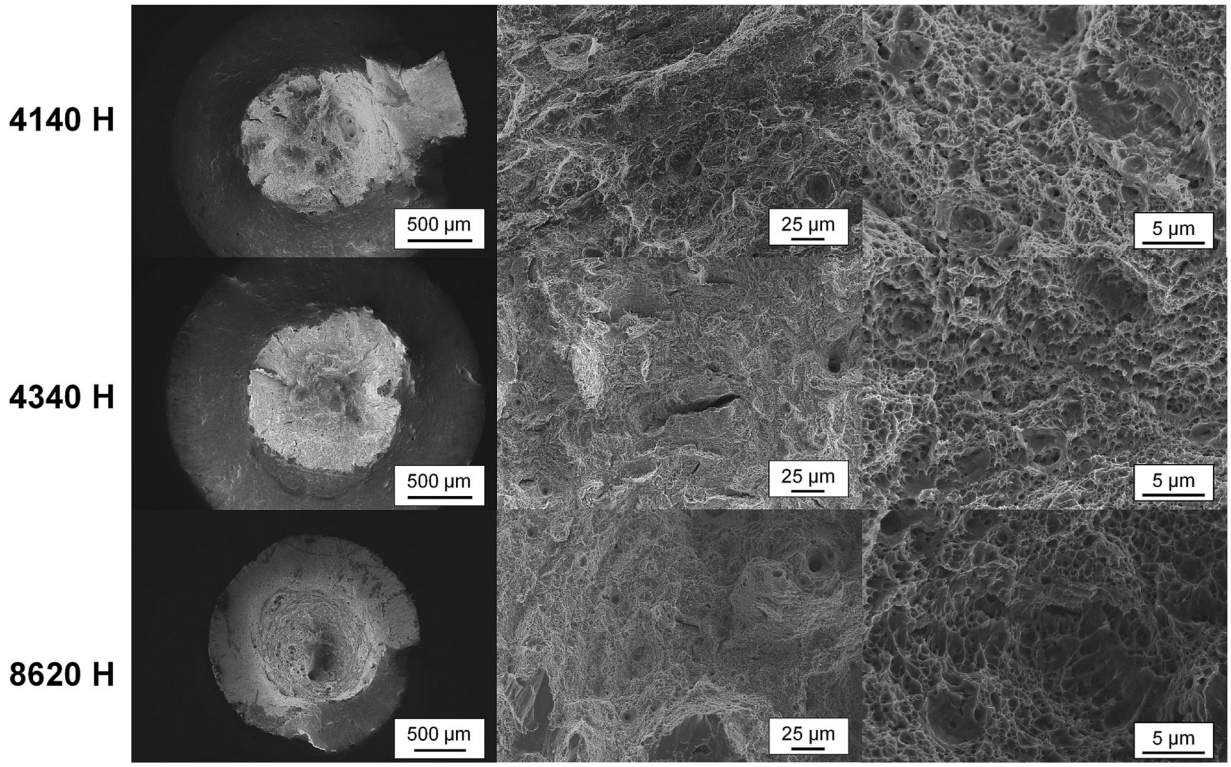

Figure 8. Fracture surfaces from horizontal tensile specimens at magnifications of 100x, 1kx and 10kx. Analysis of the fracture surfaces at 1kx revealed a few scattered pores as well as some secondary cracks in the AISI 4140 and 4340 alloys. While analysis at 10kx revealed many fine dimples across the fracture surfaces.

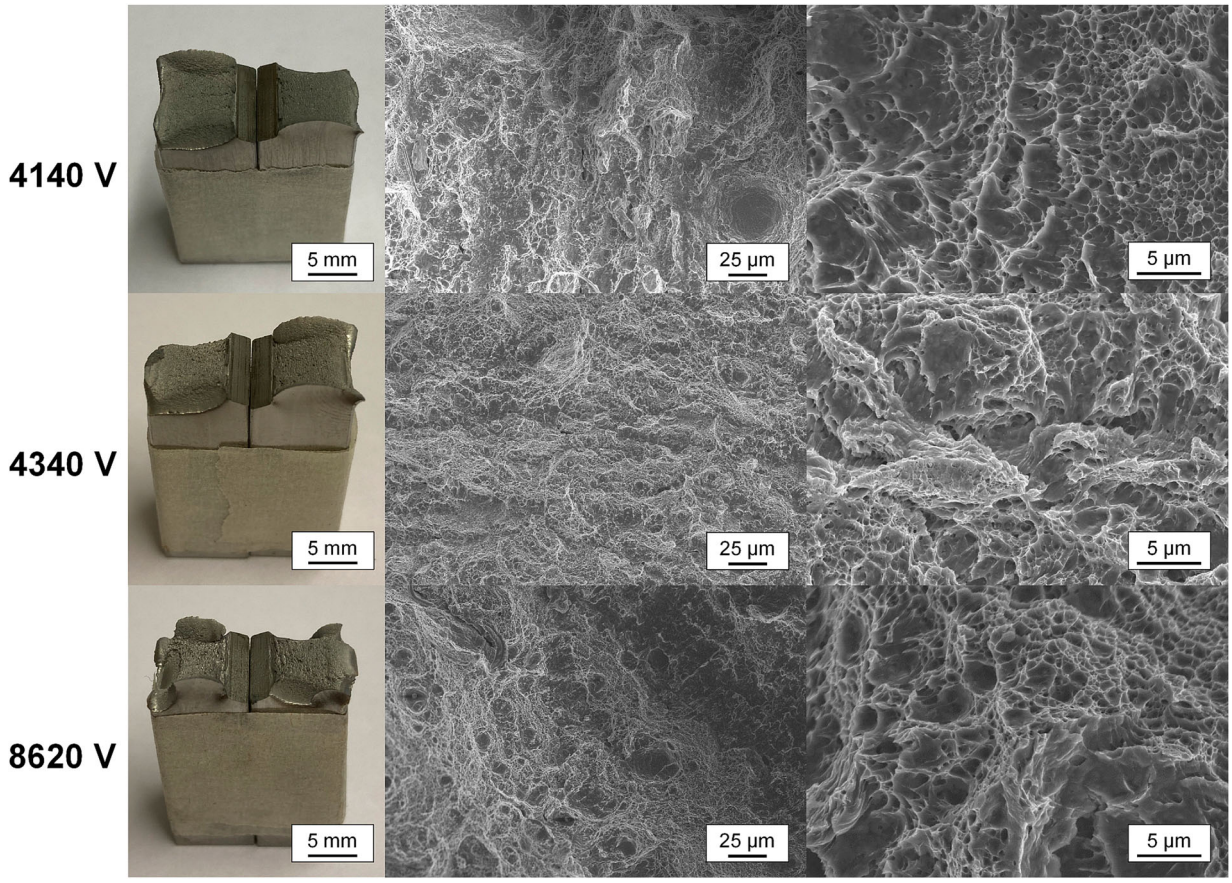

Figure 9. Fracture surfaces from vertical Charpy specimens. SEM images of the fracture surface show magnifications of 1kx and 15kx. Analysis of the fracture surfaces at 1kx revealed a few scattered pores. While analysis at 15kx revealed many fine dimples across the fracture surfaces.

impact toughness was notably exceptional, as in many cases it exceeded that of conventionally produced AISI 4140 [25], AISI 4340 [26,27] and AISI 8620 steel [28] despite having a similar or higher strength.

This combination of properties was due to the microstructure of the low-alloy steels that consisted of tempered martensite and nano-sized precipitates, see Figure 10. This finely tempered microstructure allowed the alloys to retain the high strength and hardness of martensite without noticeably reducing the ductility or toughness. The observed precipitates are likely non-transitional carbides, as previous work by Hearn et al [29]. found that the precipitates observed in plain carbon steel produced by PBF-LB related to cementite. However, further phase analysis is still required using higher resolution techniques to conclusively determine the presence and type(s) of carbides within the low-alloy steels.

Another finding from mechanical property testing was the limited presence of anisotropy when comparing the horizontally and vertically produced specimens. This was in part due to the unique grain structure of the low-alloy steels. Typically, alloys processed by PBF-LB will form large columnar grains that are preferentially oriented in the direction of heat flow [1,30]. These grains subsequently lower the strength of vertically oriented specimens, as the loading direction will be perpendicular to these elongated grains [31]. However, in this work a different grain structure was observed as instead of large elongated grains, the alloys were comprised of fine martensite laths and small columnar/equiaxed parent austenite grains, see Figure 11. There was also a lack of crystallographic texture within the examined low-alloy steels, see Figure 12. Similar findings were observed in martensitic maraging steel produced by PBF-LB [32], where the lack of crystallographic texture was attributed to the 67° scan rotation angle during laser exposure. However, the lack of texture is also due to the characteristics of the martensitic transformation, that involve the athermal nucleation and growth of martensite into a multitude of variants whose preferred orientation is independent of the heat flow direction [33]. Combined, the smaller grains and weaker texture of the examined low-alloy steels contributed to the reduced levels of anisotropy within the produced specimens.

Another cause for the limited anisotropy was the enhanced uniformity of martensite tempering due to build plate preheating and post PBF-LB stress relief. This uniformity was observed from hardness measurements that showed limited differences in specimen hardness in terms of orientation, see Table 4, as well as limited deviations in hardness within each specimen, see Figure 14. Although this subject has not been directly explored in literature, past studies have shown that heat treatment after processing can improve the mechanical properties of additively manufactured specimens [31]. These results indicate the

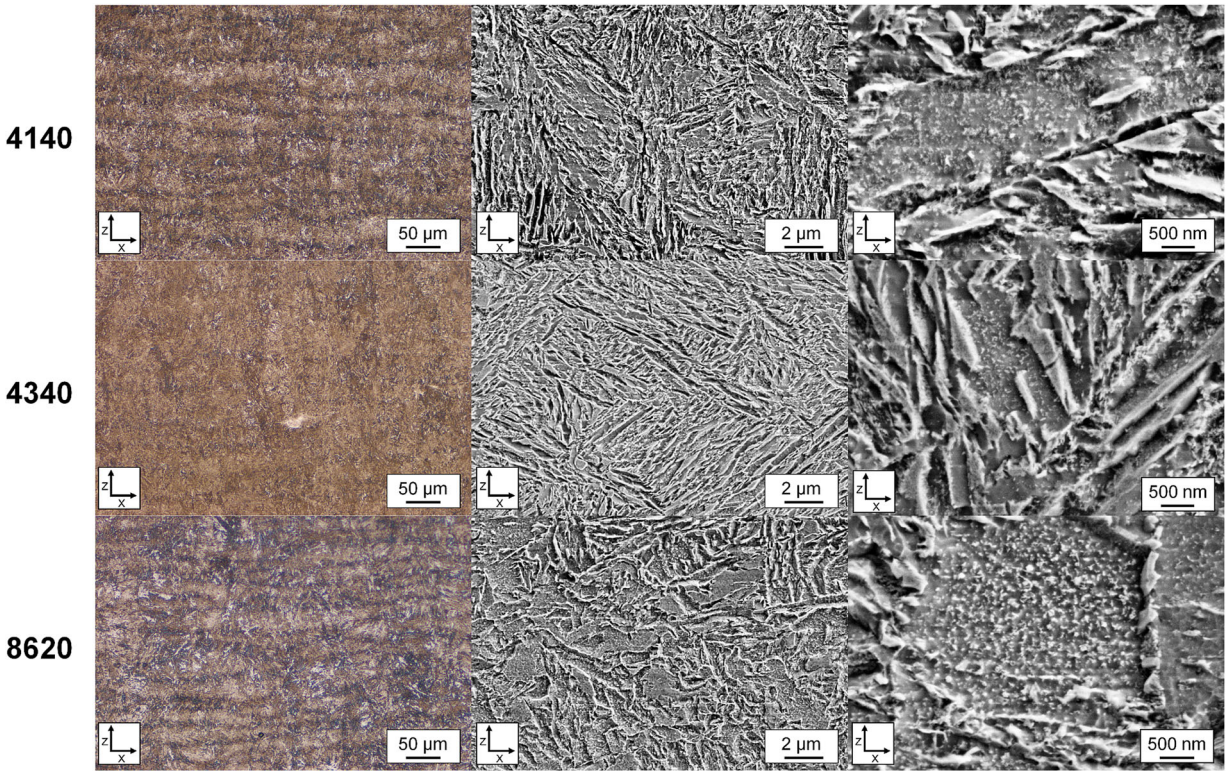

Figure 10. OM and SEM images of the AISI 4140, 4340 and 8620 alloys at magnifications of 20x, 15kx and 50kx. OM images at 20x revealed a martensitic structure. 15kx SEM images showcase the lath-like morphology of martensite. While the 50kx SEM images highlight the presence of nano-precipitates within the martensite.

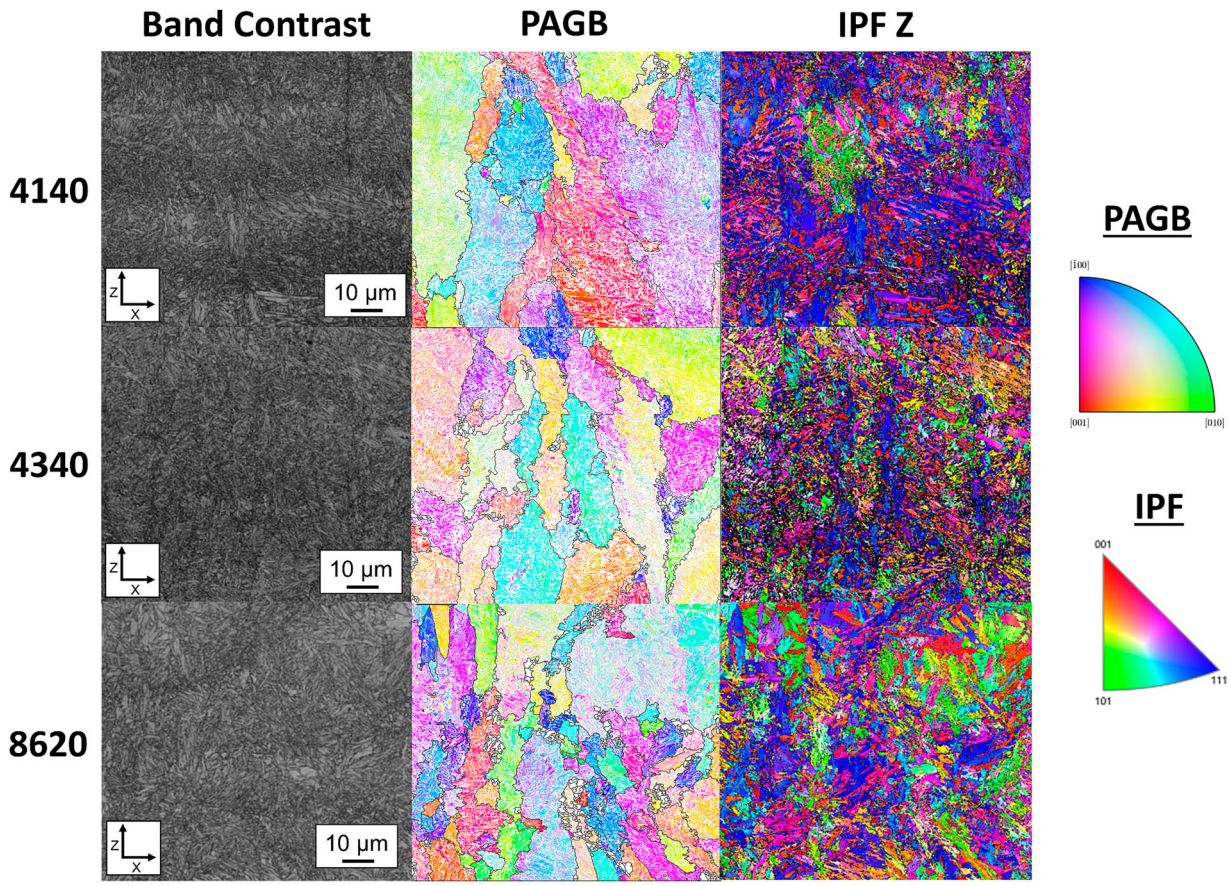

Figure 11. Representative EBSD images of AISI 4140, 4340 and 8620 alloys found in vertically produced tensile specimens. These include: (i) Images of the band contrast, (ii) Reconstruction of the parent austenite grains as calculated by MTEX [18], and (iii) Inverse pole figure (IPF) mapping of martensite in the building direction (z-axis).

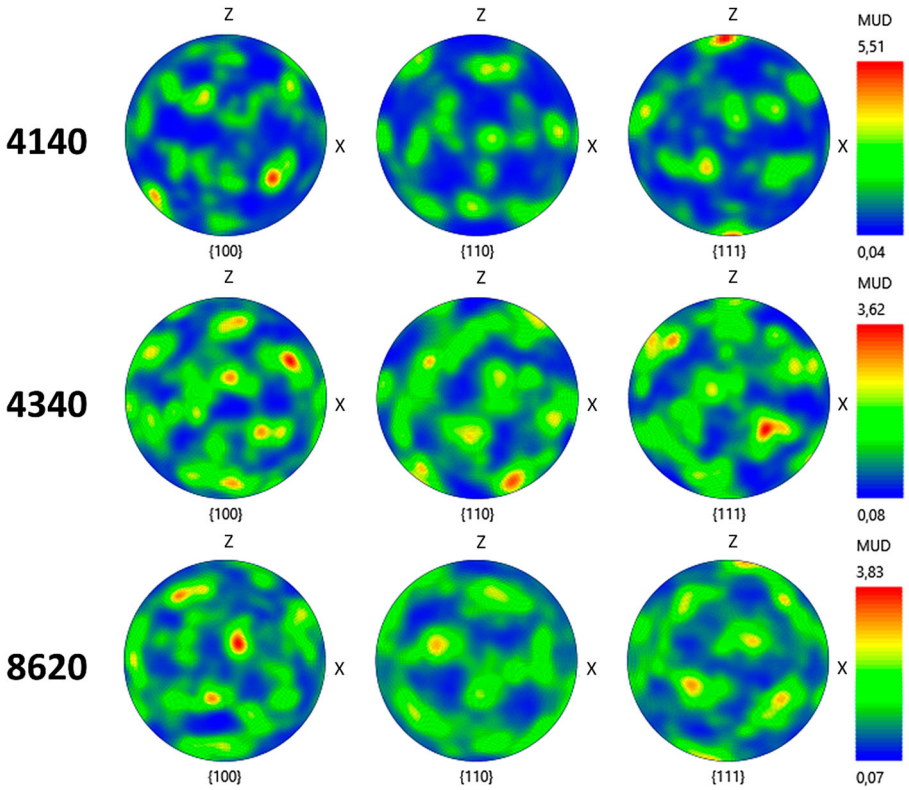

Figure 12. Pole figures for AISI 4140, 4340 and 8620 alloys that correspond to the EBSD data shown in Figure 11. These pole figures do not show strong texture and instead point to a more random crystallographic orientation.

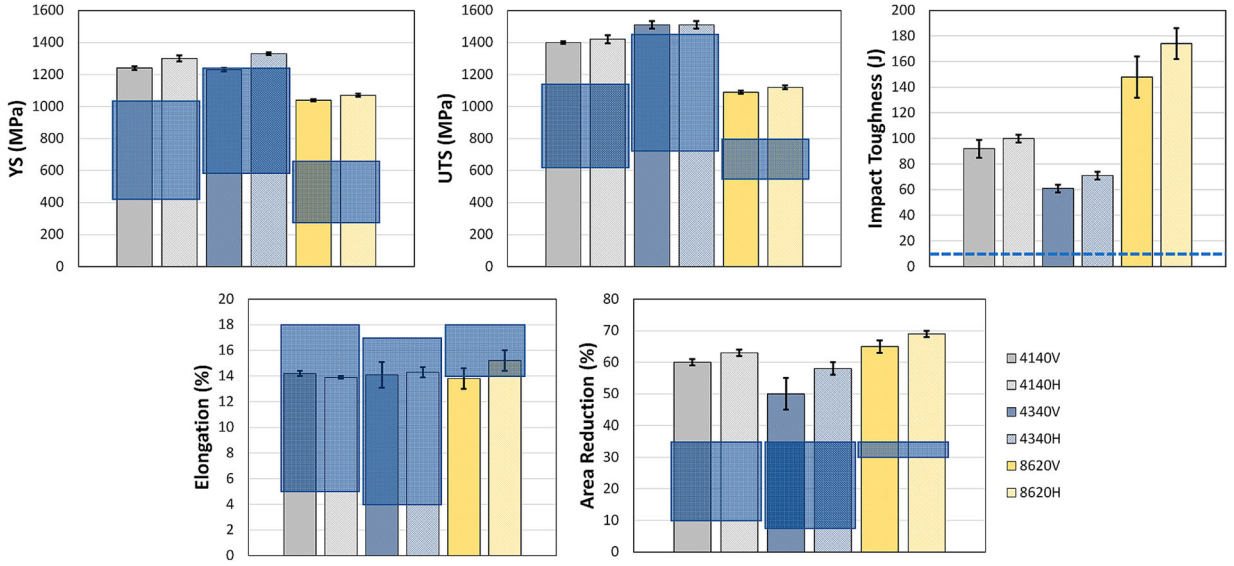

Figure 13. Mechanical properties of the AISI 4140, 4340 and 8620 alloys compared to the ASTM standards (highlighted as boxed regions or as dashed lines). The ASTM standards for the yield strength (YS), ultimate tensile strength (UTS), elongation and area reduction were taken from the ASTM A958 standard [36]. While the ASTM standard for the impact toughness was taken from the ASTM A673 standard [37].

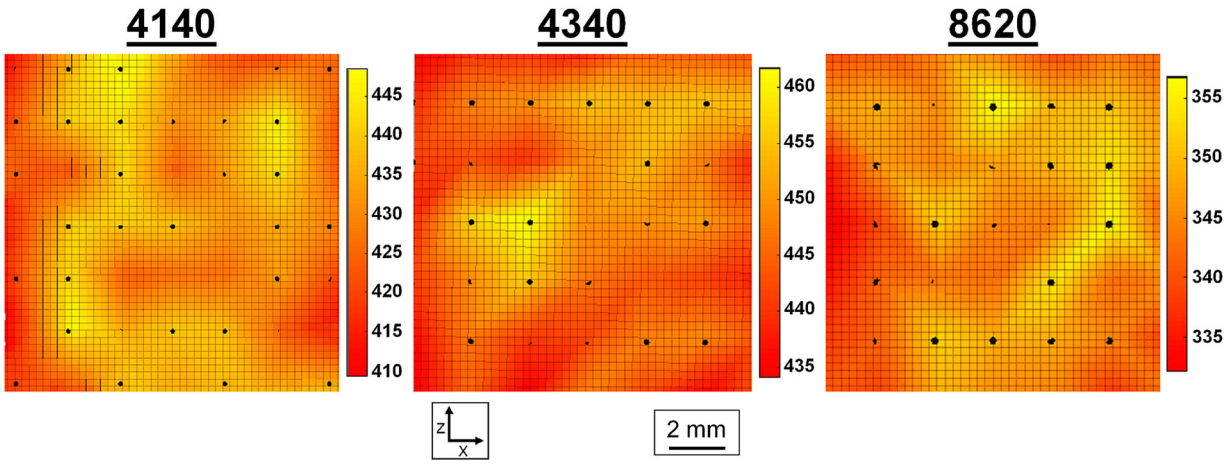

Figure 14. Hardness mapping of horizontal Charpy specimens for the AISI 4140, 4340 and 8620 alloys. This mapping revealed relatively uniform hardness throughout each specimen, with the maximum difference in hardness for each alloy reaching up to 8%, 6% and 7% respectively.

potential of build plate preheating as well as post PBF-LB stress relief to limit directional anisotropy.

Lastly, the limited presence of internal defects (< 0.1%) also contributed to the reduced levels of anisotropy, as previous studies have shown that defects oriented perpendicular to the loading direction are one of the major factors that reduce the mechanical properties of PBF-LB materials [34,35].

Conclusions

In this study, a combination of process development and mechanical property testing was conducted to evaluate the performance of AISI 4140, 4340 and 8620 low-alloy steel when using PBF-LB. The main findings of this study can be summarised as follows:

- Lack of fusion defects can be significantly decreased, and cold cracking defects can be mitigated by increasing the VED and the BPT as both parameters improve material bonding and in-situ tempering of the alloys respectively.
- The investigated alloys could be produced high-density (> 99.8%) and defect-free by PBF-LB, with the most robust processing window being found at a BPT of 180°C.
- Mechanical property testing found that the low-alloy steels had a high ultimate tensile strength (AISI4140: ~1400 MPa, AISI 4340: ~1500 MPa, AISI 8620: ~1100 MPa), impact toughness (AISI 4140: ~90–100 J, AISI 4340: ~60–70 J, AISI 8620: ~150–175 J) and elongation (AISI 4140: ~14%, AISI 4340: ~14%, AISI 8620: ~14–15%).

- Mechanical testing also revealed limited directional anisotropy. This was attributed to the reduced presence of internal defects, the prevalence of small grains with limited crystallographic texture and the improvement in martensite tempering due to build plate preheating and post PBF-LB stress relief.

In summary, this investigation has shown that when processed defect-free and high-density, martensitic low-alloy steels are not only suitable but actively take advantage of PBF-LB to achieve mechanical properties that meet or exceed those of conventionally produced alloys.

Acknowledgements

This study was conducted in the frame of the Centre for Additive Manufacturing – Metal (CAM^2), supported by the Swedish Governmental Agency of Innovation Systems (Vinnova).

Disclosure statement

No potential conflict of interest was reported by the author (s).

Funding

The work was performed in the framework of the Centre for Additive Manufacturing – Metal (CAM^2), supported by the Swedish Governmental Agency of Innovation Systems (Vinnova).

Notes on contributors

William Hearn is currently a Ph.D. student at the Centre for Additive Manufacturing – Metal (CAM^2) hosted by the Department of Industrial and Materials Science at Chalmers University of Technology, Gothenburg, Sweden. His work focuses on material development for powder-based additive manufacturing technologies.

Peter Harlin is currently a research leader at Sandvik Additive Manufacturing as well as an adjunct senior lecturer in the Division of Subtractive and Additive Manufacturing at University West, Trollhättan, Sweden.

Eduard Hryha is a professor in Powder Metallurgy and Additive Manufacturing in the Department of Industrial and Materials Science at Chalmers University of Technology, Gothenburg, Sweden. He is also the director of the Competence Centre for Additive Manufacturing – Metal (CAM^2), hosted by the same department. His research focuses on powder metallurgy and powder-based metal additive manufacturing.

ORCID

William Hearn http://orcid.org/0000-0001-9106-7945

References

[1] DebRoy T, Wei H, Zuback J, et al. Additive manufacturing of metallic components – process, structure and properties. Prog Mater Sci. 2018;92:112–224. doi:10.1016/j.pmatsci.2017.10.001.

[2] Priarone P, Lunetto V, Atzeni E, et al. Laser powder bed fusion (L-PBF) additive manufacturing: On the correlation between design choices and process sustainability. Procedia CIRP. 2018;78:85–90. doi:10.1016/j.procir.2018.09.058.

[3] Dossett J, Totten G. ASM handbook, volume 04D - heat treating of irons and steels. Materials Park (OH): ASM International; 2014.

[4] Committee AIH. ASM handbook, volume 01 - properties and selection: irons, steels, and high-performance alloys. Materials Park (OH): ASM International; 1990.

[5] Seede R, Zhang B, Whitt A, et al. Effect of heat treatments on the microstructure and mechanical properties of an ultra-high strength martensitic steel fabricated via laser powder bed fusion additive manufacturing. Add Manuf. 2021;47; doi:10.1016/j.addma.2021.102255.

[6] Jelis E, Clemente M, Hespos M, et al. Round robin study evaluating consistency of 4340 steel. J Mater Eng Perform. 2021;30:6832–6843. doi:10.1007/s11665-021-06020-8.

[7] Jelis E, Hespos M, Ravindra N. Process evaluation of AISI 4340 steel manufactured by laser powder Bed fusion. J Mater Eng Perform. 2018;27:63–71. doi:10.1007/s11665-017-2989-8.

[8] Seede R, Shoukr D, Zhang B, et al. An ultra-high strength martensitic steel fabricated using selective laser melting additive manufacturing: densification, microstructure, and mechanical properties. Acta Mater. 2020;186:199–214. doi:10.1016/j.actamat.2019.12.037.

[9] Ryder M, Mongomery C, Brand M, et al. Melt pool and heat treatment optimization for the fabrication of high-strength and high-toughness additively manufactured 4340 steel. J Mater Eng Perform. 2021;30:5426–5440. doi:10.1007/s11665-021-05836-8.

[10] Li X, Hao Tan Y, Willy H, et al. Heterogeneously tempered martensitic high strength steel by selective laser melting and its micro-lattice: processing, microstructure, superior performance and mechanisms. Mater Des. 2019;178:1–13. doi:10.1016/j.matdes.2019.107881.

[11] Dilip J, Janaki Ram G, Starr T, et al. Selective laser melting of HY100 steel: process parameters, microstructure and mechanical properties. Add Manuf. 2017;13:49–60. doi:10.1016/j.addma.2016.11.003.

[12] Wang W, Kelly S. A metallurgical evaluation of the powder-Bed laser additive manufactured 4140 steel material. JOM. 2016;68(3):869–875. doi:10.1007/s11837-015-1804-y.

[13] Narvan M, Al-Rubaie KS, Elbestawi M. Process-structure-property relationships of AISI H13 tool steel processed with selective laser melting. Materials (Basel). 2019;12:1–20. doi:10.3390/ma12142284.

[14] Mertens R, Dadbakhsh S, Van Humbeeck J, et al. Application of base plate preheating during selective laser melting. Procedia CIRP. 2018;74:5–11. doi:10.1016/j.procir.2018.08.002.

[15] Kempen K, Vrancken B, Buls S, et al. Selective laser melting of crack-free high densit M2 high speed steel parts by baseplate preheating. J Manuf Sci Eng. 2014;136:1–6. doi:10.1115/1.4028513.

[16] Schneider C, Rasband W, Eliceiri K. NIH image to ImageJ: 25 years of image analysis. Nat Methods. 2012: 671–675. doi:10.1038/nmeth.2089.
[17] Hearn W, Steinlechner R, Hryha E. Laser-based powder bed fusion of non-weldable low-alloy steels. Powder Metall. 2021. doi:10.1080/00325899.2021.1959695.
[18] Niessen F, Nyssönen T, Gazder A, et al. Parent grain reconstruction from partially or fully transformed microstructures in MTEX. ArXiv Prepr. ArXiv2104.14603. 2021.doi:10.48550/arXiv.2104.14603.
[19] "ASTM E8M/E8M-21: Standard Test Methods for Tension Testing of Metallic Materials," ASTM International, 2021.
[20] "ASTM E2298-18: Standard Test Method for Instrumented Impact Testing of Metallic Materials," ASTM International, 2018.
[21] Hearn W, Hryha E. Effect of carbon content on the processability of Fe-C alloys produced by laser based powder Bed fusion. Front Mater. 2022;8; doi:10.3389/fmats.2021.800021.
[22] Thampy V, Fong A, Calta N, et al. Subsurface cooling rates and microstructural response during laser based metal additive manufacturing. Sci Rep. 2020;10; doi:10.1038/s41598-020-58598-z.
[23] Mertens R, Vrancken B, Holmstock N, et al. Influence of powder bed preheating on microstructure and mechanical properties of H13 tool steel SLM parts. Phys Procedia. 2016;83:882–890. doi:10.1016/j.phpro.2016.08.092.
[24] Narvan M, Ghasemi A, Fereiduni E, et al. Part deflection and residual stresses in laser powder bed fusion of H13 tool steel. Mater Des. 2021;204:109659. doi:10.1016/j.matdes.2021.109659.
[25] Meysami A, Ghasemzadeh R, Seyedein S, et al. An investigation on the microstructure and mechanical properties of direct-quenched and tempered AISI 4140 steel. Mater Des. 2010;31:1570–1575. doi:10.1016/j.matdes.2009.09.040.
[26] Saeglitz M, Krauss G. Deformation, fracture, and mechanical properties of low-temperature-tempered martensite in SAE 43xx steels. Metall Mater Trans A. 1997;28:377–387. doi:10.1007/s11661-997-0139-x.
[27] Materkowski J, Krauss G. Tempered martensite embrittlement in SAE 4340 steel. Metall Trans A. 1979;10:1643–1651. doi:10.1007/BF02811697.
[28] Boyle E, Northwood D, Bowers R, et al. The effects of initial microstructure and heat treatment on the core mechanical properties of carburized automotive steels. Mater Forum. 2008;32:44–54.
[29] Hearn W, Lindgren K, Persson J, et al. In situ tempering of martensite during laser powder bed fusion of Fe-0.45C steel. Materialia. 2022;23:101459. doi:10.1016/j.mtla.2022.101459.
[30] Haghdadi N, Laleh M, Moyle M, et al. Additive manufacturing of steels: a review of achievements and challenges. J Mater Sci. 2021;56:64–107. doi:10.1007/s10853-020-05109-0.
[31] Kok Y, Tan X, Wang P, et al. Anisotropy and heterogeneity of microstructure and mechanical properties in metal additive manufacturing: a critical review. Mater Des. 2018;139:565–586. doi:10.1016/j.matdes.2017.11.021.
[32] Tan C, Zhou K, Kuang M, et al. Microstructural characterization and properties of selective laser melted maraging steel with different build directions. Sci Technol Adv Mater. 2018;19:746–758. doi:10.1080/14686996.2018.1527645.
[33] Bajaj P, Hariharan A, Kini A, et al. Steels in additive manufacturing: a review of their microstructure and properties. Mater Sci Eng A. 2020;772; doi:10.1016/j.msea.2019.138633.
[34] Åkerfeldt P. Additive manufacturing of Ti-6Al-4V: relationship between microstructure, defects and mechanical properties. Luleå: Luleå University of Technology; 2016.
[35] Larrosa N, Wang W, Read N, et al. Linking microstructure and processing defects to mechanical properties of selectively laser melted AlSi10Mg alloy. Theor Appl Fract Mech. 2018;98:123–133. doi:10.1016/j.tafmec.2018.09.011.
[36] "ASTM A958/A958M - 17: Standard specification for steel castings, carbon and alloy, with tensile requirements, chemical requirements similar to Standard Wrought Grades," ASTM International, 2017.
[37] "ASTM A673/A673M - 17: Standard specification for sampling procedure for impact testing of structural steel," ASTM International, 2017.